Available online at www.sciencedirect.com
SCIENCE DIRECT®
International Journal of Heat and Mass Transfer 48 (2005) 5121–5133
International Journal of HEAT and MASS TRANSFER
www.elsevier.com/locate/ijhmt

Melting and oxidation behavior of in-flight particles in plasma spray process

Hong-Bing Xiong [a,*], Li-Li Zheng [a], Li Li [b], Anirudha Vaidya [b]

[a] Department of Mechanical Engineering, State University of New York at Stony Brook, Stony Brook, NY 11794, United States
[b] Department of Materials Science and Engineering, State University of New York at Stony Brook, Stony Brook, NY 11794, United States

Received 30 July 2004; received in revised form 30 July 2005
Available online 26 September 2005

Abstract

The melting and oxidation behavior of in-flight particles and their effects on the splat formation are studied. An order-of-magnitude analysis and one-dimensional thermal resistance analysis are employed to investigate the heat and mass transport from the plasma flame to the particle. Two dimensionless parameters, "melting index" and "oxidation index" are derived to characterize the melting status and the oxide content of the in-flight particles, respectively. These two indice are correlated with experimentally measurable parameters, such as particle size, velocity, temperature and spray distance. Numerical simulations and experimental results are discussed to validate the analytic solutions. Effects of particle size on the melting and oxidation behavior are also investigated.

Keywords: Melting; Oxidation; Plasma spray

1. Introduction

Plasma spray is such a process in which a large amount of powders are injected into a hot flame jet, being heated and accelerated to the substrate. This process has been widely used to produce metallic and ceramic coatings. The particle motion and heating is of vital importance for process control and design, since the in-flight particle characteristics greatly influence the splat formation and coating properties. A number of models have been developed on this subject that require considering many special effects under plasma conditions [1–7]. However, most of these models used lumped thermal analysis for particles and ignored the phenomena of mass transport and chemical reaction. Particle melting and oxidation behavior were not fully understood.

The melt fraction of the particles upon impact will affect the splat morphology and coating properties significantly, especially for low-thermal-conductivity materials, such as ceramic in thermal barrier coating (TBC). Although it has not fully proved theoretically, the role of partially melted particle in molten droplet spreading and solidification are expected to be in two folds [8], the unmelted part may enhance the dissipation of the kinetic energy and thus slow down the spreading process; and the unmelted part may also bounce away from the substrate and then introduce the disturbance that favors

* Corresponding author. Tel.: +1 631 632 8346; fax: +1 631 632 8544.
E-mail address: lili.zheng@stonybrook.edu (H.-B. Xiong).

0017-9310/$ - see front matter © 2005 Elsevier Ltd. All rights reserved.
doi:10.1016/j.ijheatmasstransfer.2005.07.019

Nomenclature

Bi	Biot number, $Bi = hr_p/k_l$
Bi_m	mass transfer Biot number, $Bi_m = r_p h_m/\rho_l D_{o,l}$
C_p	specific heat, J kg^{-1} K^{-1}
C_D	drag coefficient
D_o	diffusion coefficient of oxygen, m^2 s^{-1}
Fo	Fourier number, $Fo = \alpha_l t/r_p^2$
Fo_m	mass transfer Fourier number, $Fo = D_{o,l} t/r_p^2$
h	convective heat transfer coefficient, W m^{-2} K^{-1}
h_m	mass transfer coefficient, kg m^{-2} s^{-1}
k	thermal conductivity, W m^{-1} K^{-1}
L	latent heat of fusion, J kg^{-1}
Pr	Prandtl number, $Pr = \nu/\alpha$
r_p	particle radius, μm
Re_p	Reynolds number, $2\rho_f r_p \lvert \mathbf{U}_f - \mathbf{U}_p \rvert/\mu_f$
Sc	Schmidt number, $Sc = \nu/D_o$
S	spray distance, cm
Ste	Stefan number, $Ste = C_p(T_s - T_m)/L$
t	time, ms
T	temperature, K
T_m	melting point, K
T_s	particle surface temperature, K
$\mathbf{U}$	velocity vector, m s^{-1}
Y_o	oxidant concentration

Greek symbols

μ	viscosity, kg s^{-1} m^{-1}
ρ	density, kg m^{-3}

Subscripts

f	flame
l	liquid
ox	oxide
p	particle
s	solid

particle splashing. Therefore, the presence of partially melted particles may result in a high fragmented splat, low deposition efficiency and high coating porosity.

The oxidation of atmospheric sprayed metal particles can also greatly affect the coating property and performance. In some applications, oxidation is detrimental [9]. For example, the coating corrosive resistance is reduced due to the brittleness of the oxide and the mismatch of the thermal expansion coefficients; and the low wettability of the oxide layer is responsible for the poor intersplat cohesion in the metal coatings. Therefore, a reliable description of the melting and oxidation behavior of the sprayed particle is essential to improve the understanding of the relationship between the in-flight particles characteristics and the coating properties; this will certainly help develop an effective control of the coating efficiency and quality.

Some research has been conducted to understand the in-flight particle melting in various thermal spray processes [3,10]. The effects of melt fraction on splat morphology, however, are not fully understood. Vaidya et al. [11] conducted an experimental investigation of the splat morphology over a wide range of particle conditions. A "melting index", given as $T_p \cdot t/2r_p$, was used to indicate the particle melting state based on its in-flight temperature, residence time and size. This parameter was further refined by Zhang et al. through the energy balance analysis and correlated with the splat morphology after impact [8]. Efforts have also been made to investigate the in-flight particle oxidation and its influences on coating property. The amount and distribution of the oxide formed in the particles in-flight have been observed by different researchers [12–15]. The oxidation mechanisms have also been studied numerically by Wan et al. [16] and Ahmed et al. [17] based on the mass transport and chemical reaction during particle in-flight.

This paper presents analysis and characterization of the melting and oxidation behavior of in-flight particles. Two practical parameters, melting and oxidation indices, are derived to estimate the melt fraction and the oxide content, respectively. Values of these two indices are validated by the three-dimensional simulation results for representative ceramic (ZrO_2) and metal (Mo) powder materials. In particular, the melting index of ZrO_2 particles and its relationship with the deposition rate and splat morphology will be discussed in terms of experimental data.

2. Mathematical model

2.1. Particle melting index

Coating is an assemble of splats formed on the substrate and the splat morphologies are directly related to the coating properties. Fig. 1 shows SEM pictures of splats formed by partially and fully melted ceramic particle. The experimental data revealed that the particle melting status before impact affects the splat morphology. For a partially melted particle, splat is formed in such a way—only melted part of particle sticks well to the substrate. To qualitatively identify the melting status of the particle, the scaling analysis is conducted to the heat and mass transfer for particles in a plasma heated environment as shown in Fig. 2(a). The analysis is based on the assumptions such that the particle is spherical, and

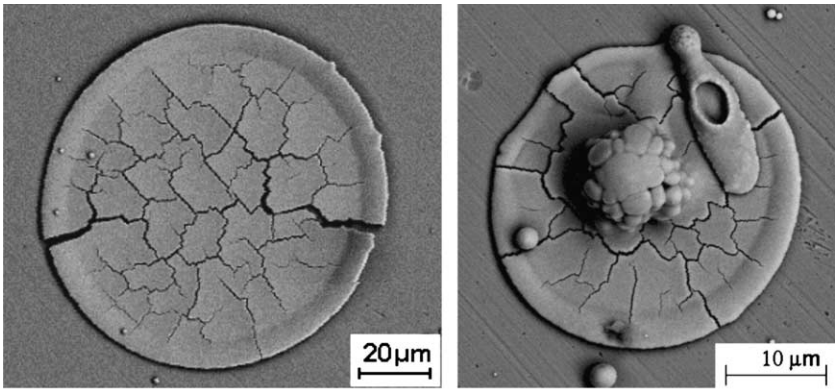

Fig. 1. SEM picture of the splat formed (a) by a totally melted zirconia particle and (b) by a partially melted zirconia particle.

heat transfer inside particles is conduction dominated; the particle is primarily heated up by surrounding plasma gas through convection. The schematic of particle geometry and important heat transfer modes are shown in Fig. 2(b). It shall be noted that once particles are entrained into the plasma hot core, their surfaces are heated up rapidly and reach the melting point in a short time (approximately 0.1 ms) [3]. And this heating time is negligible compared to the melting time required for the latent heat dissipating from the particle surface to the center for ceramic particles. From the thermal resistance analysis [18], the relationship between the surface temperature, T_s, the melting temperature, T_m, and the flame temperature, T_f, can be obtained as follows:

$$\frac{T_f - T_m}{T_s - T_m} = \frac{R_1 + R_2}{R_1}, \tag{1}$$

where R_1 and R_2 are the thermal resistances by conduction and convection, respectively. Based on spherical particle geometry, $R_1 = \frac{1}{4\pi k_1}\left(\frac{1}{r} - \frac{1}{r_p}\right)$ and $R_2 = \frac{1}{4\pi r_p^2 h}$. If $T_f - T_m = 1000$ K is assumed, $T_s - T_m = 60$ K and 3.2 K are derived for in-flight ZrO_2 and Mo particles, respectively, using heat transfer coefficient, $h = 1500$ W/m^2 K, particle diameter of 50 μm, and unmelted core diameter of 10 μm. Different values for $(T_s - T_m)$ are attributed to a high thermal conductivity of Mo, 46 W/m K, compared to a low thermal conductivity of ZrO_2, 2.32 W/m K. A large temperature difference between the surface and the melt front is an important characteristic for melting a ceramic particle.

For a metal particle, the temperature is virtually uniform inside the particle due to its high thermal conductivity. Thus the particle surface temperature can be used to identify the phase status of the particle. Also due to the high thermal diffusivity of a metal particle, it is easy for a particle to be heated up in the plasma jet to the melting temperature and being melted. For a ceramic particle, the particle temperature changes from a high value at its surface to a low value at its center; and high temperature at the particle surface does not guarantee the particle being fully melted. This is attributed to its low thermal conductivity and high melting point; at which conditions, the particle being injected into a plasma flame may not be melted completely even if the surface temperature of the particle is much higher than the melting temperature. The melting percentage of the particle depends on its size, thermal conductivity, latent heat, and residence time in the plasma flame. A melting index is therefore needed to determine the melting behavior of a particle.

Defining a dimensionless parameter—melting index M.I. as a ratio of the time for particle in-flight, Δt_{fly}, to the time required for a particle fully melted, Δt_{melt}. Based on the thermal resistance analysis, the total time required for a particle being fully melted, is estimated analytically. For most plasma spray conditions, the Biot number for powder particle is small. The temperature distribution in the solid phase is negligible. Thus, the total heat transferred to the particle melt and solid interface shall be balanced with the latent heat absorbed by particle for melting. This is described mathematically as follows:

$$q'' = \dot{m}L = \frac{T_f - T_m}{R_1 + R_2} = \frac{T_f - T_m}{\frac{1}{4\pi k_1}\left(\frac{1}{r} - \frac{1}{r_p}\right) + \frac{1}{4\pi r_p^2 h}}, \tag{2}$$

where L is the latent heat of fusion, and $\dot{m} = -4\rho\pi r^2 \frac{dr}{dt}$. Substituting $\dot{m}$ into Eq. (2),

$$-\rho \cdot 4\pi r^2 \frac{dr}{dt} \cdot L = \frac{T_f - T_m}{\frac{1}{4\pi k_1}\left(\frac{1}{r} - \frac{1}{r_p}\right) + \frac{1}{4\pi r_p^2 h}} \tag{3}$$

is obtained. It shall be noted that the convection heat transfer coefficient h and the flame temperature T_f vary

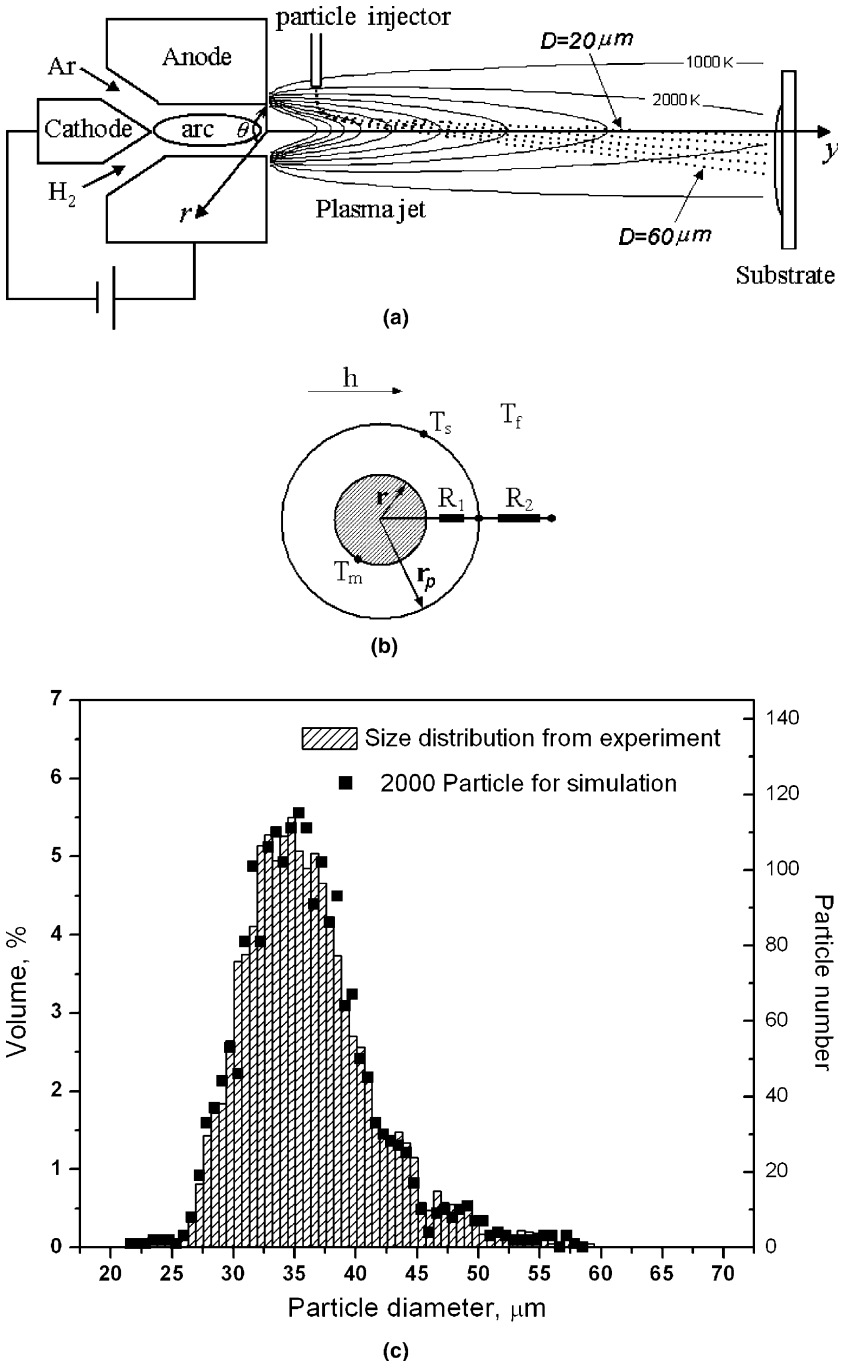

Fig. 2. (a) Schematic of plasma spraying process using a DC plasma torch, (b) schematic of the in-flight particle melting process, and (c) initial particle size distribution from sieving experiment and data used in simulations.

with particle location. Nevertheless, their variations along the particle trajectory under most normal plasma spray conditions are not significant for the given gun power. Eq. (3) can thus be integrated and the total melting time is derived as follows:

$$\Delta t_{\text{melt}} = \frac{r_{\text{p}}^2}{6}\left(1+\frac{2}{Bi}\right)\cdot\frac{\rho L}{k_{\text{l}}(T_{\text{f}}-T_{\text{m}})} \tag{4}$$

in which $Bi = hr_{\text{p}}/k_{\text{l}}$. The melting time for ZrO_2 particles with radius of 25 and 50 μm are estimated as 2.1 ms and

Table 1
Particle properties

Particle material	ZrO_2	Mo
k_s, W m^{-1} K^{-1}	2.0	84
k_l, W m^{-1} K^{-1}	2.32	46
$C_{p,s}$, J kg^{-1} K^{-1}	580	339
$C_{p,l}$, J kg^{-1} K^{-1}	713	570
ρ_s, kg m^{-3}	5.89×10^3	10.0×10^3
ρ_l, kg m^{-3}	5.89×10^3	9.35×10^3
T_m, K	2950	2895
L, J kg^{-1}	7.07×10^5	3.71×10^5

30 ms, respectively; while the melting time for Mo particles with these two radii are about 0.028 ms and 0.11 ms, respectively. In this estimation, $h = 1500$ W/m^2 K and $T_f - T_m = 3000$ K are used along with the particle properties listed in Table 1. Apparently, a metal particle melts much faster than a ceramic particle of equivalent size. With Eq. (4), the melting index can be formulated as follows:

$$\text{M.I.} = \frac{\Delta t_{fly}}{\Delta t_{melt}} = \frac{6k_l}{\rho L}\cdot\frac{1}{1+2/Bi}\cdot\frac{(T_f - T_m)\cdot\Delta t_{fly}}{r_p^2}. \quad (5)$$

2.2. Particle oxidation index

Molybdenum (Mo) is a metal material used to spray wear-resistant coatings. In atmospheric plasma spray, Mo is easily to be melted because of its high thermal conductivity. However, the plasma spraying of metals in atmospheric environment inevitably leads to oxide formation, which will degrade the Mo coatings. To control oxidation of metal particles in-flight, the oxidation behavior of Mo particles is studied here. Different oxidation mechanisms should be considered for different material and in different stage of particle temperature. For example, Wan et al. [16] considered three oxidation mechanisms for Molybdenum particle: diffusion in an oxide thin film at a surface temperature lower than 450 °C, chemical reactions at temperature higher than 500 °C, and adsorption of oxidant diffused from the gas to the surface when the particle is melted. Their results showed that the primary oxidation mechanism for Mo particle in-flight is the adsorption after particle melting since the reaction rates of the two former mechanisms are very small, usually below 10^{-3} kg/m^2 s. Therefore we only considered the primary oxidation mechanism that the oxidant diffuses from the gas to the melted surface and reacts with the metal particle. This mechanism can be represented by

$$\text{Mo} + \frac{x}{2}\text{O}_2 \Longleftrightarrow \text{MoO}_x. \quad (6)$$

The oxide phase will be formed and well separated from the metal phase due to the difference of the surface tension. SEM images obtained by Espie et al. [13] in the atmospheric plasma spray showed that the collected in-flight iron particles have distinguishable oxide grains, $Fe_{0.95}O$. As indicated in Fig. 3(a), a large oxide nodule is typically formed within the particle, and some small oxide nodules are distributed around it. To reduce the complexity of the problem, we assume that the oxides form a large nodule and are located at the particle center, as shown in Fig. 3(b). From the resistance analysis, the relationship among the oxygen concentration on the particle surface, $Y_{o,s}$, in the particle center, $Y_{o,c}$, and in the gas phase, $Y_{o,f}$, can be obtained as follows:

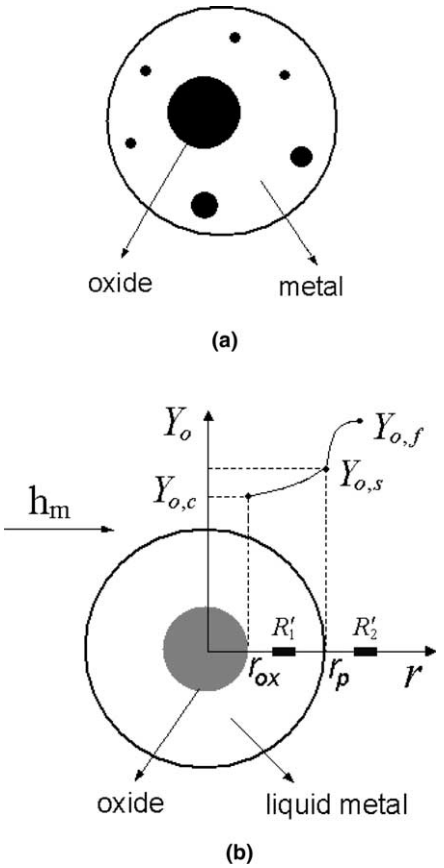

Fig. 3. Schematic of the in-flight particle oxidation process: (a) cross-section of an oxidized particle and (b) mass transfer and diffusion of oxidant through the particle.

$$\frac{Y_{o,f} - Y_{o,c}}{Y_{o,f} - Y_{o,s}} = \frac{R_1' + R_2'}{R_2'} = 1 + Bi_m\left(\frac{r_p}{r} - 1\right), \quad (7)$$

where R_1' and R_2' are the mass transfer resistances by diffusion and convection, respectively. Bi_m in Eq. (7) is the mass transfer Biot number, $Bi_m = r_p h_m/\rho_l D_{o,l}$. Based on the spherical geometry for particles, $R_1' = \frac{1}{4\pi\rho_l D_{o,l}}\left(\frac{1}{r} - \frac{1}{r_p}\right)$, and $R_2' = \frac{1}{4\pi r_p^2 h_m}$. If $Y_{o,f} - Y_{o,c} \approx Y_{o,f} = 0.4$ is assumed, $Y_{o,s} = 0.04$ and 0.2 are derived for $Bi_m = 0.025$ and

0.25, respectively using the particle diameter of 50 μm and the oxide nodule diameter of 10 μm. The concentration of oxygen at the particle surface is a strong function of mass transfer Biot number, and the particle in-flight oxidation process is either diffusion-in-melt controlled for large Bi_m case, or mass-transfer-in-gas controlled for small Bi_m case. Note that for large Bi_m, e.g., greater than 1, the concentration of oxygen in the melted surface might reach the solubility of oxygen in the liquid Mo.

The oxidant flux at the particle surface can be expressed as follows:

$$m''_o = \frac{Y_{o,f} - Y_{o,c}}{R'_1 + R'_2} = m''_{ox}\frac{W_o}{W_{ox}}, \tag{8}$$

where W_o and W_{ox} are the atomic weights of the oxidant and the oxide product, and $m''_{ox} = \rho_{ox}4\pi r^2\frac{dr}{dt}$. Substituting m''_{ox} into Eq. (8),

$$\rho_{ox}4\pi r^2\frac{dr}{dt} = \frac{Y_{o,f} - Y_{o,c}}{\frac{1}{4\pi\rho_l D_o}\left(\frac{1}{r} - \frac{1}{r_p}\right) + \frac{1}{4\pi r_p^2 h_m}}\cdot\frac{W_{ox}}{W_o} \tag{9}$$

is obtained. Eq. (9) can be integrated and the oxide nodule size, r_{ox}, can be obtained as follows:

$$\frac{r_{ox}^2}{2} + \frac{r_{ox}^2}{3r_p}\left(\frac{1}{Bi_m} - 1\right) = (Y_{o,f} - Y_{o,c})D_{o,l}\frac{W_{ox}}{W_o}\frac{\rho_l}{\rho_{ox}}t. \tag{10}$$

To quantify the intensity of the oxidation in the partile, an oxidation index, O.I., is introduced in this article. It is defined as the ratio of the oxide weight m_{oxide} to the particle weight $m_{particle}$ as follows:

$$\text{O.I.} = \frac{m_{oxide}}{m_{particle}} = \frac{(Y_{o,f} - Y_{o,c})D_o\frac{W_{ox}}{W_o}t}{r_p^2\left[\frac{r_p}{2r_{ox}} + \frac{1}{3}\left(\frac{1}{Bi_m} - 1\right)\right]}. \tag{11}$$

If Bi_m is much larger than one, the mass transfer resistance by diffusion in the liquid droplet becomes dominant. This leads to $Y_{o,f} \approx Y_{o,s} \gg Y_{o,c}$. Eq. (11) can be simplified to

$$\text{O.I.} = (Y_{o,f} - Y_{o,c})D_o\frac{W_{ox}}{W_o}\frac{t}{r_p^2(B/2 - 1/3)}, \tag{12}$$

where B is the ratio of the particle radius to the oxide nodule radius, r_p/r_{ox}. If Bi_m is much smaller than one, the mass transfer in the gas phase will be dominant, and $Y_{o,f} \gg Y_{o,s} \approx Y_{o,c}$. Eq. (11) can be simplified to

$$\begin{aligned}\text{O.I.} &= 3h_m(Y_{o,f} - Y_{o,c})\frac{W_{ox}}{W_o}\frac{t}{\rho_l r_p}\\ &= 3\frac{W_{ox}}{W_o}\cdot Bi_m\cdot(Y_{o,f} - Y_{o,c})\cdot Fo_m.\end{aligned} \tag{13}$$

Therefore, more oxide will be formed for the small convective mass transfer resistance (large Bi_m), long flight time (large Fo_m), and/or high oxygen concentration in the environment (large $Y_{o,f}$).

2.3. Determination of heat and mass transfer coefficients

In Eqs. (5) and (13), the heat and mass transfer coefficients between the particle surface and the environment, h and h_m, are unknown. These parameters depend on plasma jet conditions, particle size and trajectory. Thus numerical simulations have been performed to determine their values using a well-tested and validated code—LAVA–P–3D [3,4,16,19]. A DC (direct current) plasma spraying process, as displayed in Fig. 2(a), has been simulated using the operating conditions listed in Table 2, with the powder materials of ZrO_2 and Mo, respectively. The initial particle size distribution used in the simulations is shown in Fig. 2(c), along with the original sampling experimentally obtained by sieving. Volume fraction (90%) of the particles has the diameter in the range of 28–44 μm.

The current LAVA–P–3D code treats the plasma jet as a compressible, continuous multi-component, chemically reacting ideal gas with temperature-dependent thermodynamic and transport properties. The governing equations of mass, species, momentum and energy conservations in cylindrical coordinate have been solved. Detailed descriptions of the governing equations and numerical solutions can be referred to Ref. [18].

The particle is treated as a discrete Lagrangian entity that exchanges mass, momentum, and energy with the gas. The movement of particles is driven by the drag force due to the velocity difference between the particle and gas. The momentum transfer between the particle and the gas can be described by:

$$\mathbf{F}_p = m_p\frac{d\mathbf{U}_p}{dt} = \pi r_p^2 C_D\frac{\rho|\mathbf{U}_f - \mathbf{U}_p|(\mathbf{U}_f - \mathbf{U}_p)}{2}, \tag{14}$$

where the drag coefficient $C_D = \left(24Re_p^{-1} + 6\left(1 + Re_p^{-1/2}\right) + 0.4\right)f_{prop}^{-0.45}f_{Kn}^{0.45}$ [1,2]. The particle's Reynolds number, $Re_p = 2\rho_f r_p|\mathbf{U}_f - \mathbf{U}_p|/\mu_f$, is less than 100. Eq. (14) is used to calculate the particle velocity and trajectory. The particle velocity is larger for higher gas velocity and for smaller particles. The local conditions of the plasma gas around the particles can then be determined including the thermal and diffusion coefficients. The heat

Table 2
Operating conditions for plasma spraying of ZrO_2 and Mo

Processing parameters	ZrO_2	Mo
Current, amp	600	500
Voltage, volt	69	60
Primary gas flow, Ar, SLM[a]	32	40
Secondary gas flow, H_2, SLM	8	7
Carrier gas flow, SLM	3	3

[a] SLM means standard liter per minute; 1 SLM = 16.67×10^{-6} m^3/s.

transfer coefficient can then be calculated from the Nusselt number as [3],

$$Nu = \frac{2hr_p}{k_f} = (2.0 + 0.6Re^{1/2}Pr^{1/3})(f_{prop})^{0.6} f_{Kn} f_v, \quad (15)$$

where f_{prop}, f_{Kn} and f_v represent the effects of variable plasma properties, non-continuum, and mass transfer due to evaporation, respectively; the formulations for f_{prop}, f_{Kn} and f_v can be referred to Wan et al. [3]. The mass transfer coefficient of oxygen from the gas to the surface can also be calculated from the Sherwood number as [3],

$$Sh = \frac{2h_m r_p}{\rho_f D_{o,f}} = 2.0 + 0.6Re^{1/2}Sc^{1/3}. \quad (16)$$

The heat and mass transfer within the particle are described by one-dimensional conduction and diffusion equations in spherical coordinate [3,16]

$$\rho_p C_p \frac{\partial T_p}{\partial t} = \frac{1}{r^2}\frac{\partial}{\partial r}\left(k_p r^2 \frac{\partial T_p}{\partial r}\right) \quad \text{and}$$
$$\frac{\partial Y_o}{\partial t} = \frac{1}{r^2}\frac{\partial}{\partial r}\left(D_{o,l} r^2 \frac{\partial Y_o}{\partial r}\right). \quad (17)$$

The boundary conditions of heat transfer at the particle center and surface are given as

$$\left.\frac{\partial T}{\partial r}\right|_{r=0} = 0 \quad \text{and}$$
$$4\pi r_p^2 \left(k_p \frac{\partial T}{\partial r}\right)\Big|_{r=r_p} = \dot{Q}_{conv} - \dot{Q}_{vap} - \dot{Q}_{rad}, \quad (18)$$

where $\dot{Q}_{conv}$, $\dot{Q}_{rad}$ and $\dot{Q}_{vap}$ accounts for the heat flux at the particle surface by convection, radiation and evaporation, which are expressed as $4\pi r_p^2 h(T_f - T_s)$, $4\pi r_p^2 \varepsilon\sigma(T_s^4 - T_\infty^4)$ and $\dot{m}_v L_v$ respectively. Only the radiation between the particle surface and the environment is considered in the case of optically thin plasma gas. Similarly, the boundary conditions of mass transfer at the particle center and surface are given as

$$\left.\frac{\partial Y_o}{\partial r}\right|_{r=0} = 0 \quad \text{and} \quad \rho_p D_{o,l} \left.\frac{\partial Y_o}{\partial r}\right|_{r=r_p} = h_m(Y_{o,f} - Y_{o,s}). \quad (19)$$

The melting interface is treated as an internal moving boundary between the two different phase domains. The boundary conditions are given as

$$T_i = T_m \quad \text{and}$$
$$\left(k_{p,s}\left.\frac{\partial T}{\partial r}\right|_{r=r_m^-}\right) - \left(k_{p,l}\left.\frac{\partial T}{\partial r}\right|_{r=r_m^+}\right) = \rho_p L \frac{dr_m}{dt}. \quad (20)$$

3. Experimental data

The experimental data from the literature [11] have been used to validate the numerical results and investigate the melting index of ZrO_2 particles. Their experiments use a PTF 4MB DC plasma gun, with operating conditions listed in Table 2 (the case of ZrO_2). The partially stabilized zirconia (PSZ) AE7592 from Sulzer-Metco, which is a plasma densified hollow spherical powder (HOSP), with a mean size of 36 μm is used as the feedstock. The particle injector is located at 0.6 cm away from the torch exit. The experimental data for in-flight particles and splats are collected at the spray distance of 6, 8, 10 and 12 cm, respectively. The Tecnar DPV 2000 diagnostic system is used to measure the in-flight particle size, velocity and surface temperature. Splats are collected on mirror polished 304 stainless steel (roughness <0.1 μm). A large number (70) of splats are scanned by the scanning white light interferometry, Zygo New Viewer 200.

4. Results and discussion

4.1. Melting index

To evaluate the particle heat transfer coefficient, numerical results have been obtained and compared with the experimental data. Fig. 4 shows the numerical results of axial velocity, surface temperature and melting status for ZrO_2 particles for different sizes. It reveals that a small particle has a high axial velocity and a high surface temperature. All particles start melting virtually at the same location of 0.8 cm, regardless of the size. They are totally melted after a flight distance of 1.1, 1.8, 3 and 5.5 cm for particles with initial diameters of 20, 30, 40, and 50 μm, respectively. The latent heat of fusion and thermal resistance are responsible for the different flight time for different size of particles being fully melted.

The simulation results of average axial velocity and surface temperature, are also shown in Fig. 4 (see straight lines) for the particles with size distributions of Fig. 2(c). The experimental results measured from the DPV2000, are shown by square symbols in Fig. 4. The simulation results agree reasonably well with the experiment in consideration of the uncertainty in the measurements. Note that the measured velocity decreases significantly between the spray distance of 6 cm and 12 cm, while the simulation results show that the particle velocity is virtually constant after certain spray distance. This discrepancy is attributed to the fact that the DPV2000 tends to "see" large and hot particles better. After the spray distance beyond 6 cm, the DPV2000 is no longer sensible to the small particles that cool down rapidly.

To interpret the particle melting process analytically, we need to estimate the particle flight time, the flame temperature and the heat transfer coefficient using the simulation results. The simulation results in Fig. 4(a) shows that particles experience the motion with constant acceleration in most flight distance. The flight time is therefore

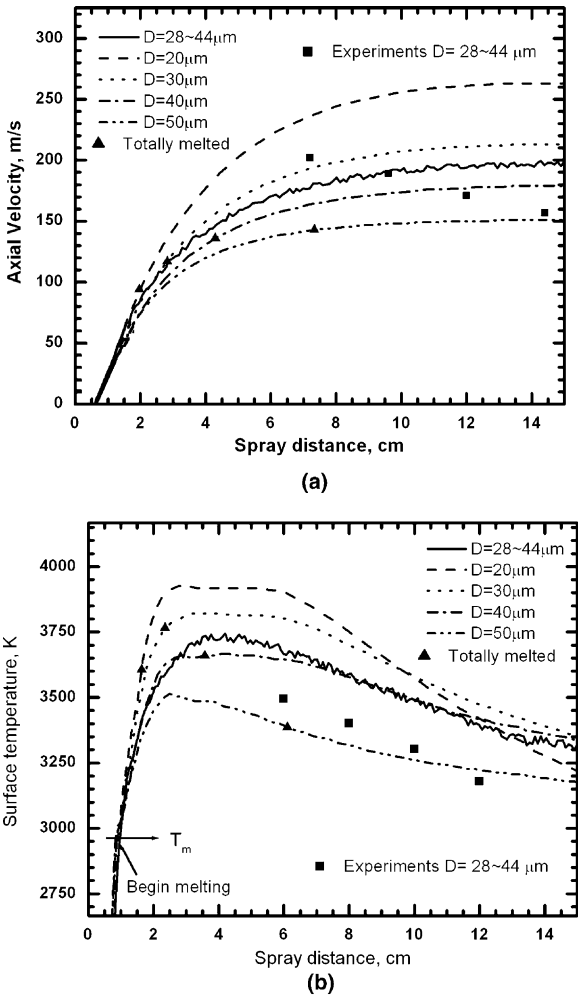

Fig. 4. (a) Particle velocity and (b) surface temperature for different sizes of ZrO_2 particles, with experimental data.

approximated as $\Delta t_{\mathrm{fly}} = 2S/V_{\mathrm{p}}$, where S is the axial flight distance and V_{p} is the particle axial velocity.

Fig. 5 shows the heat transfer coefficient h and the flame temperature T_{f} during the melting process of ZrO_2 particles. The heat transfer coefficient is related to the particle size, Reynolds number and the flame gas thermal conductivity. The results show that h varies within a small range during particle melting for a given size. The averaged values are 3.5, 3.2, 2.6, 2.2, and 2.1×10^4 W m^{-2} K^{-1} for particles with initial diameters of 20, 30, 40, 50 and 60 μm, respectively. These values have been used to calculate the melting index.

The particles with different sizes experience different flame temperature, since each particle undergoes its own trajectory. Small particles experience low flame temperature as they cannot penetrate the flame center easily. This is seen schematically in Fig. 2(a). On the contrary, a large particle reaches the center of the plasma flame but moves away from the hot core of the plasma jet. Since the flame temperature is related to the particle surface temperature (see Eq. (1)), we introduce a dimensionless temperature $A = (T_{\mathrm{f}} - T_{\mathrm{m}})/(T_{\mathrm{s}} - T_{\mathrm{m}})$ to estimate the flame temperature. As shown in Fig. 5(c), this dimensionless temperature behaves similarly during the melting process for particles with different sizes. Substituting Δt_{fly} and A to Eq. (5),

$$\mathrm{M.I.} = A\frac{12k_{\mathrm{l}}}{\rho L}\cdot\frac{1}{1+2/Bi}\cdot\frac{(T_{\mathrm{s}}-T_{\mathrm{m}})S}{r_{\mathrm{p}}^2 V_{\mathrm{p}}} \tag{21}$$

is obtained. Note that in the experiments, the particle surface temperature and velocity are measurable. The properties such as k_{l}, L, ρ, and T_{m} are also known for the given powder material. However, the values of A and h are unknown and they are estimated from the simulations.

Mass fraction of the melt in the particle, f, can be represented by the melting index as shown in Fig. 5(d). The melting index is calculated by Eq. (21), using the heat transfer coefficient h and dimensionless temperature A estimated by simulation (see Fig. 5(a) and (c)). When the particles are fully melted ($f = 1$), the melting index, M.I., ranges from 0.8 to 1.2 for the particles of $D = 20$–40 μm. The results of melting index deviate more from the melting fraction for large particles of $D = 50$–60 μm, since their surrounding flame temperature changes dramatically during its in-flight (see Fig. 5(c)). Therefore, the steady-state assumption for heat transfer analysis becomes questionable. This can be improved in the future by considering the transient heating and cooling process into the melting index formulation.

If the ZrO_2 particle diameter is smaller than 1 μm, the Biot number will be much smaller than one, even with an extreme high heat transfer coefficient of 10^4 W m^{-2} K^{-1} under the plasma conditions. For this case, the melting index can be further simplified as such,

$$\mathrm{M.I.} \approx A\frac{3h}{\rho L}\cdot\frac{(T_{\mathrm{s}}-T_{\mathrm{m}})\cdot\Delta t_{\mathrm{fly}}}{r_{\mathrm{p}}} = 3A\cdot Bi\cdot Ste\cdot Fo. \tag{22}$$

Eq. (22) revealed that the melting status of particle is proportional to the product of the Biot, Stefan and Fourier numbers if the convection is dominant. A better melting will be expected if more heat is convectively transferred from the surface to the particle. In general, the particles are more difficult to be melted in the high-velocity-oxy-fuel spray process because its short residence time in the flame prevents particle from receiving large amount of heat. The formulations derived in Eqs. (21) and (22) will be helpful to determining the melting behavior of the particles. Eventually, it can be used for control and optimization of spraying process.

4.2. Melting index for experiments

After validating with simulation, the melting index can be used to characterize the melting status of the

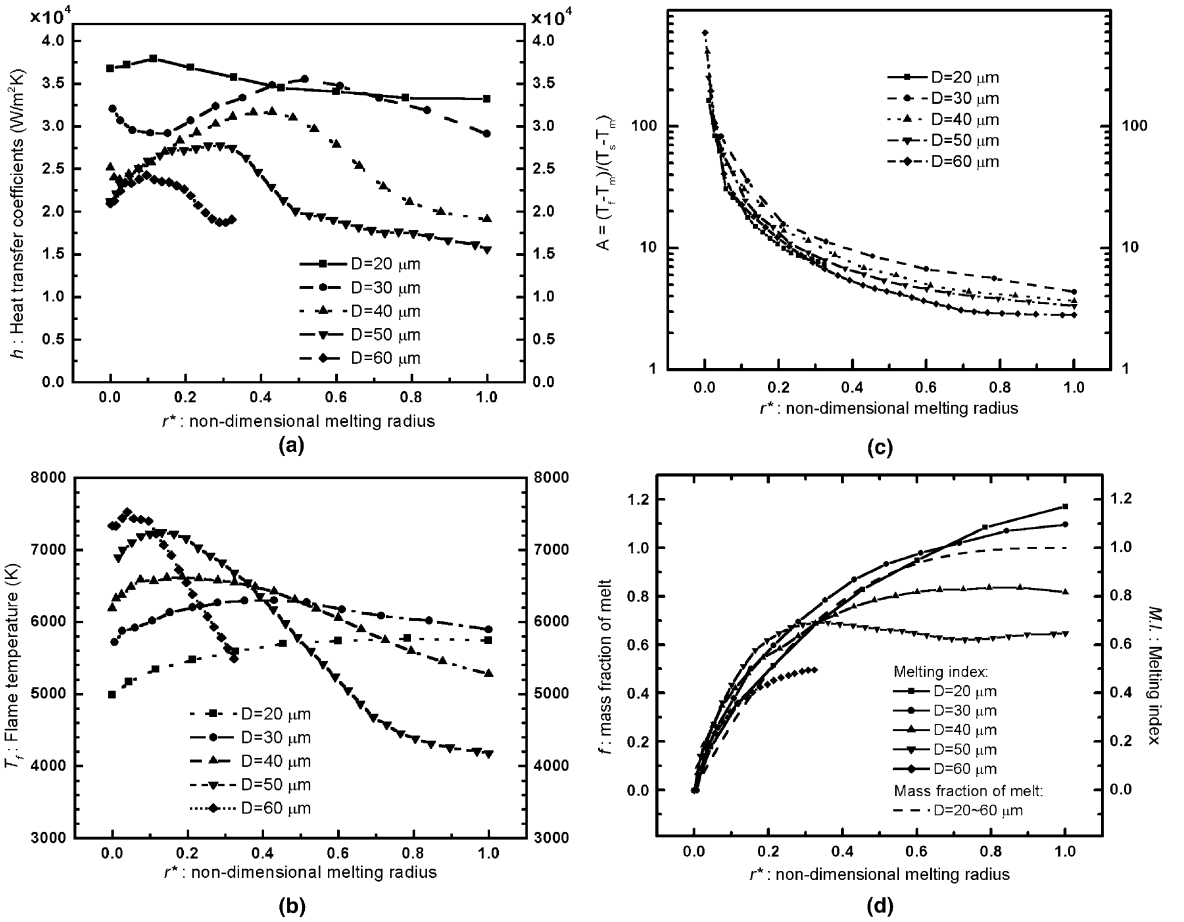

Fig. 5. (a) Heat transfer coefficient, (b) flame temperature, (c) dimensionless temperature $A = (T_f - T_m)/(T_s - T_m)$ and (d) melting index vs. the non-dimensional melting radius, $r^* = (r_p - r_m)/r_p$, for ZrO_2 particles.

in-flight particles in plasma spraying. Previous experimental studies have shown that the melt fraction of the in-flight particle has a great influence on the deposition rate and the splat morphology; a better particle melting status will increase the deposition rate [11]. The prediction of the melting is thus important for experiments. In the following, the calculation for the melting index is presented for the experiments in which the ZrO_2 particles with an averaged diameter 36 μm is plasma sprayed. The melting index is calculated by Eq. (21) with numerically estimated heat transfer coefficient ($h = 3 \times 10^4$ W m^{-2} K^{-1}) and dimensionless flame temperature ($A = 3.3$).

Fig. 6 shows the optical pictures of the collected splats, the deposition rate, and the calculated melting index based on measurable particle temperature and velocity at different spray distances. The results show a good correlation between the melting index and the splat deposition rate. This indicates that the melting index can be used to characterize the melting fraction of the ceramic particles upon impact, and can therefore be used as a control parameter to improve the spray yield. It is pointed out that the highest particle temperature is at the spray distance of 6 cm (see Fig. 4(b)), while at this location a low deposition rate of 0.06 and small melting index are obtained. This is due to the short particle flight time that does not allow particle to absorb sufficient amount of heat for melting.

The effects of the melting index on the splat morphology is also observed. The splat morphology is characterized by fragmentation degree *DS*, which presents the extent of the break up of a splat. It is defined as [8],

$$DS = P^2/(4\pi A), \tag{23}$$

where the peripheral length P and the splat area A is measured from the Zygo Viewer. *DS* equals to unit for a rigid disk-like shape splat. The splat fragmentation degree at different particle melting index and particle Reynolds number are shown in Fig. 7 [8]. The splat fragmentation degree is found to be dependent primarily on the particle

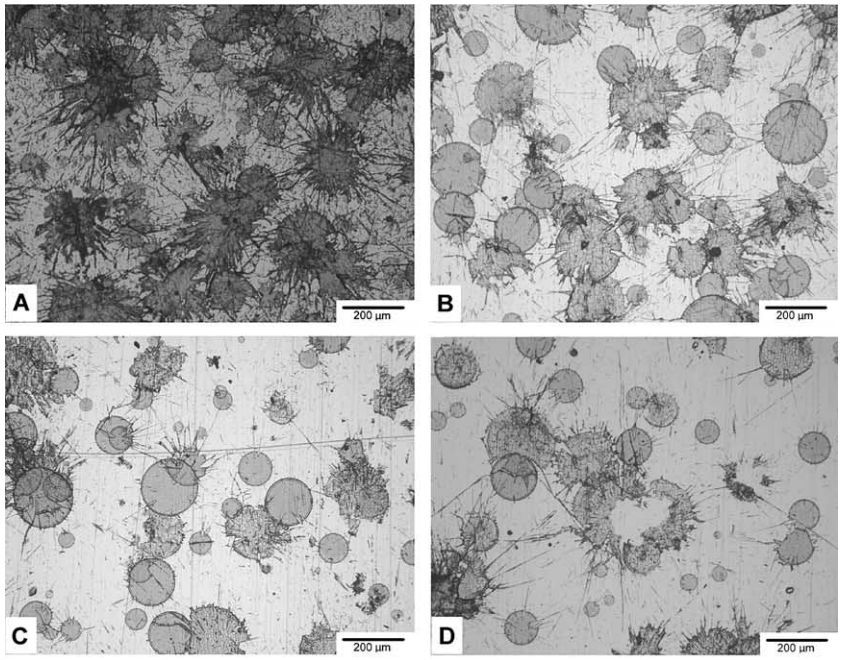

(a)

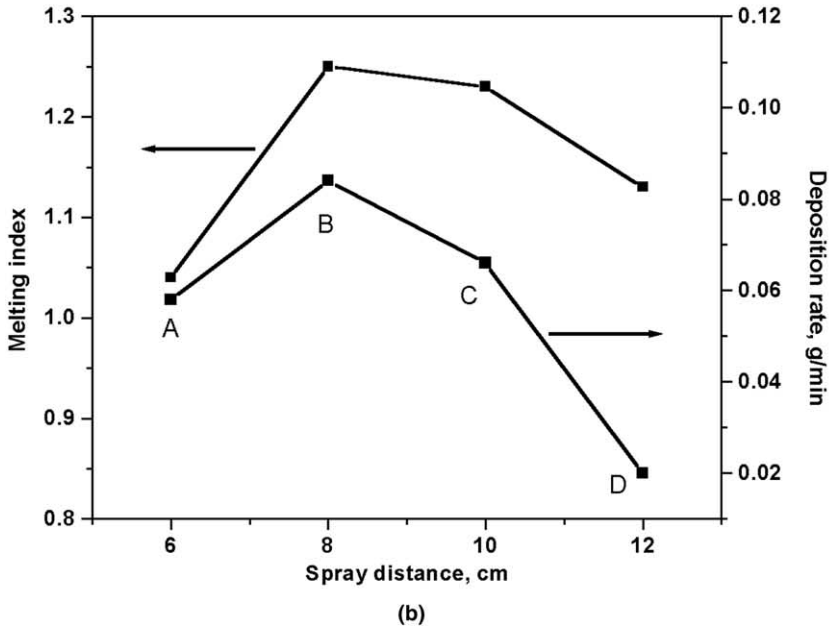

(b)

Fig. 6. (a) Optical pictures of collected splats and (b) effects of melting index on deposition rate at different spray distances of 6, 8, 10 and 12 cm.

Reynolds number, $2\rho_p V_p r_p/\mu_{p,l}$, which refers to the particle kinetic energy before impact. For the same particle Reynolds number, particle with a larger melting index will have less possibility to form fragmentation.

4.3. Oxidation index

The oxidation index, a dimensionless parameter for the metal particle oxidation behavior, is discussed in this

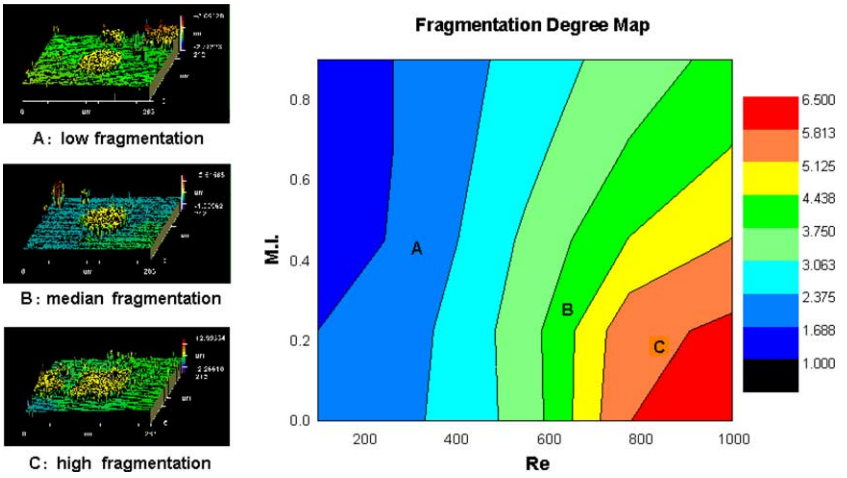

Fig. 7. Effects of melting index and particle Reynolds number on splat fragmentation degree.

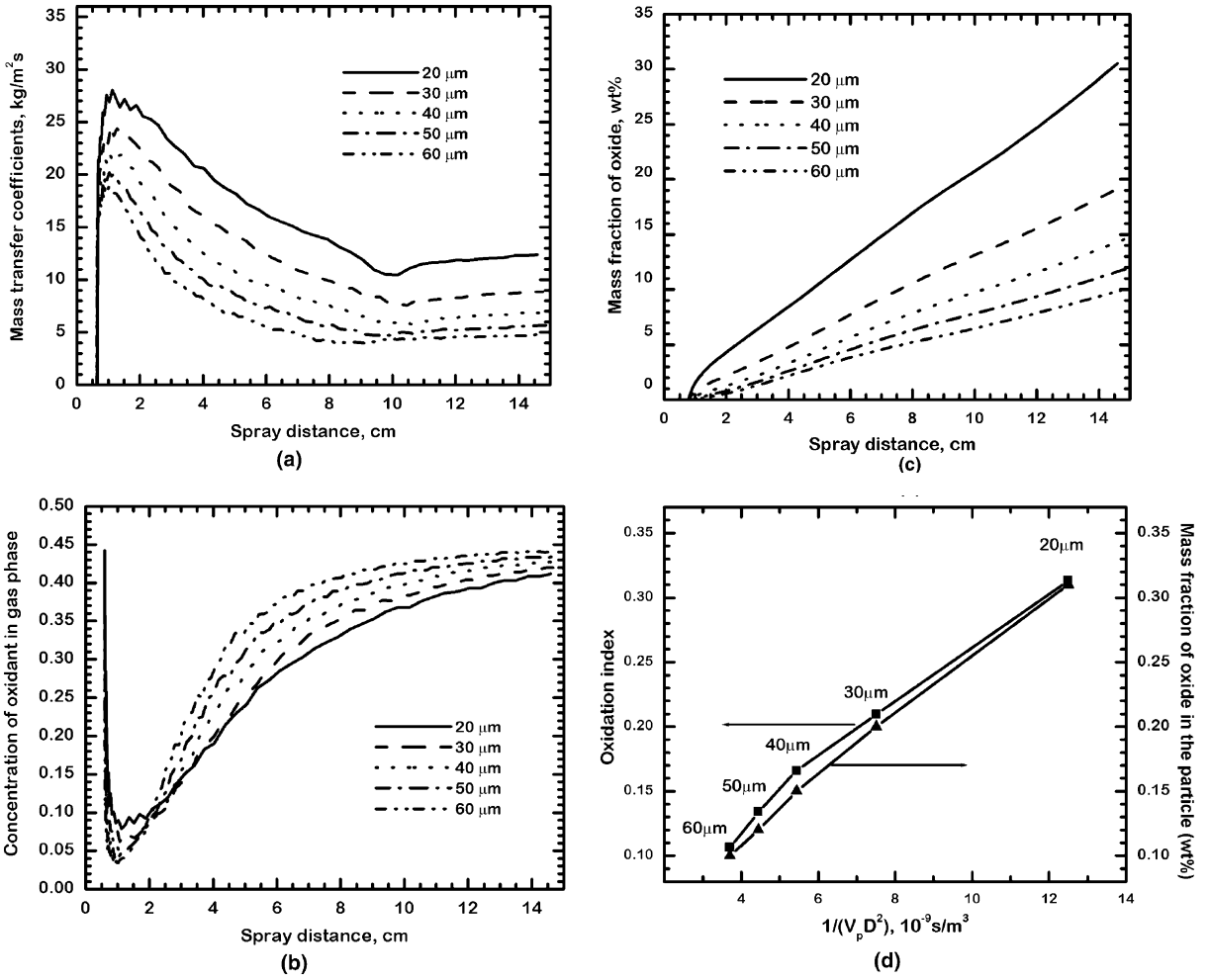

Fig. 8. (a) Mass transfer coefficient, (b) mass fraction of oxygen in the gas phase, (c) oxide content vs. spray distance, and (d) oxide content and oxidation index at the spray distance of 15 cm vs. $(V_p d_p^2)^{-1}$, for Mo particles with diameters of 20, 30, 40, 50 and 60 μm.

part using Mo as an example. The mass transfer coefficient and the oxygen concentration surrounding the particles, which are critical to the oxidation index calculation, are estimated from numerical results shown in Fig. 8(a)–(b). The mass transfer coefficient h_m increases as the particle size decreases. The oxygen concentration $Y_{o,f}$ is related to the particle trajectory and the ambient air entrainment. The oxygen concentration is small before the particle reaches the centerline (see Fig. 2(a)) as the results of small molecular oxygen (O_2) from air entrainment and atomic oxygen (O) from dissociation. The averaged values of h_m and $(Y_{o,f} - Y_{o,c})$ are 12.9, 10.6, 9.0, 7.5, 6.5 kg m^{-2} s^{-1}, and 0.28, 0.28, 0.28, 0.29, 0.30 for particles with initial diameters of 20, 30, 40, 50 and 60 μm, respectively. These values have been used to calculate the oxidation index.

The numerical results of the mass fraction of oxide formed during particles in-flight are shown in Fig. 8(c). For this study, only MoO_3 phase is assumed to be formed. Smaller particles contain more oxide. This results from the large mass transfer coefficient and the large surface to volume ratio. The mass fraction of oxide at the spray distance of 15 cm is compared with the analytical results of the oxidation index, as shown in Fig. 8(d). The oxidation index is calculated by Eq. (13), using the averaged mass transfer coefficient h_m and oxygen concentration $Y_{o,f}$. The results show that the oxidation index agrees well with the oxide mass fraction predicted from the numerical simulations, indicating that the analytical oxidation index interprets the oxide content correctly.

If the oxidation time t can be estimated as the flight time $\Delta t_{fly} = 2S/V_p$, Eq. (13) can be rewritten as such,

$$\text{O.I.} \approx \frac{6(Y_{o,f} - Y_{o,c})}{\rho_l} \frac{W_{ox}}{W_o} \frac{Sh\rho_f D_{o,f}}{d_p} \frac{S}{V_p d_p} \propto \frac{S}{V_p d_p^2}, \quad (24)$$

where Sh is defined in Eq. (16), $D_{o,f}$ is the diffusion coefficient of the oxygen in the plasma flame, and ρ_f is the averaged gas density around the particle. It reveals that the oxide content increases monotonically with the spray distance, and decreases with the particle size and velocity. This analytical conclusion is validated by the numerical simulation results (see Fig. 8(c)–(d)). The oxide content at the spray distance of 15 cm is proportional to $(V_p d_p^2)^{-1}$, which agrees well with the prediction of Eq. (24). Currently we have no experimental data regarding to the metal particle oxidation in atmospheric plasma spraying. However, such experiments have been conducted by other groups, and the similar results have been achieved. For example, the experiments with iron particles in atmospheric plasma spraying showed that the oxide content increases with the spray distance monotonically [13]. This result agrees well with our simulation result depicted in Fig. 8(c), as well as the analysis of the oxidation index. The oxidation index, Eq. (24), also shows that in-flight particles oxidation can be reduced if proper measure is taken, such as to shorten the spray distance, to reduce the number of small particles in the feedstock, or to minimize the oxygen entrainment by low pressure plasma spray or inert plasma spray.

5. Conclusions

Dimensionless group parameters, melting index and oxidation index, have been defined to describe particle melting status and in-flight particle oxide content based on experimentally measurable parameters. To fully melt a ceramic particle, the surface temperature should be much higher than the melting temperature due to the thermal resistance of the melt. Our analysis reveals that the total melting time is reciprocal to the particle diameter and velocity, and the metal particle oxidation during in-flight is reciprocal to particle velocity and diameter square. Numerical simulations have been used to determine the unknown parameters in the melting index and oxidation index. Effects of the initial particle diameter on melting and oxidation behavior have also been studied. Melting index is found to be well correlated with the splat deposition rate. The splat fragmentation degree is found to be dependent primarily on particle Reynolds number. For the same particle Reynolds number, particles with a larger melting index will have less possibility to form fragmentation.

Acknowledgements

This work was supported by the National Science Foundation under award No. CTS-0074589 and MRSEC program under award No. DMR-0080021.

References

[1] X. Chen, E. Pfender, Behavior of small particles in a thermal plasma flow, Plasma Chem. Plasma Process. 3 (3) (1983) 351–366.
[2] E. Pfender, Y.C. Lee, Particle dynamics and particle heat and mass transfer in thermal plasma. Part I: the motion of a single particle without thermal effects, Plasma Chem. Plasma Process. 5 (1985) 211–237.
[3] Y.P. Wan, V. Prasad, G.-X. Wang, S. Sampath, J.R. Fincke, Model and powder particle heating, melting, resolidification, and evaporation in plasma spraying processes, J. Heat Transfer 121 (1999) 691–699.
[4] Y.P. Wan, J.R. Fincke, S. Sampath, V. Prasad, H. Herman, Modeling and experimental observation of evaporation from oxidizing molybdenum particles entrained in a thermal plasma jet, Int. J. Heat Mass Transfer 45 (2002) 1001–10015.

[5] D. Bergmann, U. Fritsching, K. Bauckhage, A mathematical model for cooling and rapid solidification of molten metal droplets, Int. J. Therm. Sci. 39 (2000) 53–62.
[6] H. Zhang, X.Y. Wang, L.L. Zheng, X.Y. Jiang, Studies of splat morphology and rapid solidification during thermal spraying, Int. J. Heat Mass Transfer 44 (2001) 4579–4592.
[7] C. Escure, M. Vardelle, P. Fauchais, Experimental and theoretical study of the impact of alumina droplets on cold and hot substrates, Plasma Chem. Plasma Process. 23 (2) (2003) 185–221.
[8] H. Zhang, H.B. Xiong, L.L. Zheng, A. Vaidya, L. Li, S. Sampath, Partially melted particle and its splat morphology, in: B.M. Marple, C. Moreau (Eds.), Advancing the Science and Applying the Technology, ASM International, Materials Park, Ohio, 2003, pp. 905–911.
[9] K. Volenik, F. Hanousek, P. Charaska, J. Ilavsky, K. Neufuss, In-flight oxidation of high-alloy steels during plasma spraying, Mater. Sci. Eng. A272 (1999) 199–216.
[10] J. He, M. Ice, E. Lavernia, Particle melting behavior during high-velocity oxygen fuel thermal spraying, J. Therm. Spray Technol. 10 (2001) 83–93.
[11] A. Vaidya, G. Bancke, S. Sampath, H. Herman, Influence of process variables on the plasma sprayed coatings: an integrated study, in: C.C. Berndt, K.A. Khor, E.F. Lugscheider (Eds.), New Surfaces for a New Millenium, ASM International, Materials Park, Ohio, 2001, pp. 1345–1349.
[12] G. Espie, P. Fauchais, B. Hannoyer, J.C. Labbe, A. Vardelle, Effect of metal particles oxidation during the APS on the wettability, heat and mass transfer under plasma conditions, Ann. New York Acad. Sci. 891 (1999) 143–151.
[13] G. Espie, P. Fauchais, J.C. Labbe, A. Vardelle, B. Hannoyer, Oxidation of iron particles during APS: effect of the process on formed oxide wetting of droplets on ceramics substrates, in: C.C. Berndt, K.A. Knor, E.F. Lugscheider (Eds.), New Surfaces for a New Millennium, ASM International, Ohio, USA, 2001, pp. 821–827.
[14] R.A. Neiser, M.F. Smith, R.C. Dykhuizen, Oxidation in wire HVOF-sprayed steel, J. Therm. Spray Technol. 7 (1998) 537–545.
[15] V.V. Sobolev, J.M Guilemany, Effect of oxidation on droplet flattening and splat-substrate interaction in thermal spraying, J. Therm. Spray Technol. 8 (1999) 523–530.
[16] Y.P. Wan, J.R. Fincke, X.Y. Jiang, S. Sampath, V. Prasad, H. Herman, Modeling of oxidation of molybdenum particles during plasma spray deposition, Metall. Mater. Trans. B 32 (2001) 475–481.
[17] A.M. Ahmed, R.H. Rangel, V.V. Sobolev, J.M. Guilemany, In-flight oxidation of composite powder particles during thermal spraying, Int. J. Heat Mass Transfer 44 (2001) 4667–4677.
[18] F.P. Incropera, D.P. DeWitt, Fundamentals of Heat and Mass Transfer, fifth ed., Wiley & Sons, Hoboken, NJ, 2001.
[19] H.B. Xiong, L.L. Zheng, S. Sampath, R. Williamson, J. Fincke, Three-dimensional simulation of plasma spray jet: effects of carrier gas flow and particle injection on plasma jet and entrained particle, Int. J. Heat Mass Transfer 47 (2004) 5189–5200.